Volume 9
Number 1
7 January 2018
Pages 1-268

Chemical Science

rsc.li/chemical-science

ISSN 2041-6539

ROYAL SOCIETY OF CHEMISTRY

EDGE ARTICLE
Xinjing Tang et al.
Caged circular siRNAs for photomodulation of gene
expression in cells and mice

ROYAL SOCIETY OF CHEMISTRY

rsc.li/chemical-science

Organic Neuromorphic Vision Devices with Multilevel Memory for Palmprint Identification

Chenxi Liu[1,2], Yongfeng Gu[3], Yongjie Ren[3], Mingyi Ding[1,2]*, Tao Deng[4]*, Harald Fuchs[5], Deyang Ji[1,2]* and Wenping Hu[2,6]

[1]Tianjin Key Laboratory of Molecular Optoelectronic Sciences, Department of Chemistry, Institute of Molecular Aggregation Science, Tianjin University, Tianjin 300072, China

[2]Key Laboratory of Organic Integrated Circuit, Ministry of Education, Tianjin University, Tianjin 300072, China

[3]National Key Laboratory of Precision Testing Technology and Instruments, Tianjin University

[4]School of Electronic and Information Engineering, Beijing Jiaotong University, Beijing 100044, China.

[5]Physikalisches Institut and Center for Nanotechnology (CeNTech), Westfälische Wilhelms-Universität Münster, Germany

[6]Tianjin Key Laboratory of Molecular Optoelectronic Sciences, Department of Chemistry, School of Science, Tianjin University, 300072, China

* Corresponding author. E-mail address: jideyang@tju.edu.cn; dengtao@bjtu.edu.cn; dingmy@tju.edu.cn

Abstract

Neuromorphic visual devices have emerged as a critical strategy to address the limitation of the von Neumann bottleneck. However, the role of interfacial molecular engineering-specifically the modulation of polar groups in polymer gate dielectrics-in shaping the performance of neuromorphic vision systems remains insufficiently explored. Herein, we report polarity-engineered hafnium oxide (HfO_2)-based phototransistors that synergistically achieve ultrahigh photodetection sensitivity and multilevel nonvolatile memory. By strategically tuning polar functional groups in polymer gate dielectrics [polyphenylene ether (PPO) and poly(4-vinylphenol) (PVP)] combined with HfO_2, we demonstrate an enhancement in photoresponsivity compared to traditional low-polarity dielectrics, alongside realistic emulation of synaptic plasticity. The optimized devices exhibit exceptional comprehensive performance, including ON/OFF ratio exceeding 10^5, cycling endurance over 700 program/erase (P/E) cycles, retention time greater than 3×10^4 s, and 256 distinct conductance states (8-bit resolution), thus setting a new benchmark for multilevel memory capacity in memory devices. When integrated with classical machine learning algorithms, these phototransistors efficiently extract discriminative optoelectronic features from CASIA-Palmprint database images, enabling reliable biometric authentication with accuracy above 98%. This work establishes fundamental molecular design principles for neuromorphic electronics and presents an energy-efficient paradigm for vision systems that unify sensing, memory, and in-situ processing, paving the way for next-generation intelligent devices.

Keywords: polarity engineering; optoelectronic memory; neuromorphic vision; multilevel storage; palmprint identification

Chemical Science Accepted Manuscript

Introduction

The physical separation of perception, processing, and memory in conventional von Neumann architectures inherently limits computational efficiency and increases power consumption, creating a bottleneck for advanced computing applications.[1-3] To overcome these limitations, bio-inspired neuromorphic systems offer a promising alternative, enabling massively parallel processing with remarkably low power consumption.[4-6] Among biological sensory systems, vision has garnered particular attention, as visual perception constitutes the primary channel for human interaction with external information.[7-9] Consequently, artificial vision systems have emerged, typically integrating photodetectors for visual capture, memory blocks for data storage, and processors for image processing and neuromorphic computations.[10-12] While significant advances have demonstrated their potential, organic vision systems possessing integrated memory and computational capabilities remain underexplored, largely due to the fundamental conflict between efficient charge transfer and stable charge capture. Existing systems often suffer from persistent limitations, including short memory retention times,[13] high operating voltages,[14] and excessive light intensity requirements.[15] To this end, polymer dielectric interfacial engineering has proven effective for tuning device performance,[16-18] where polar functional groups (PFGs) play a pivotal role in modulating interfacial charge distribution.[19-26] Studies also indicate that PFG-influenced polymer chain arrangement critically impacts dielectric properties; highly compact structures and strong intermolecular forces improve dielectric strength and insulating characteristics.[27] Furthermore, incorporating fluorinated groups into polyimide (PI) dielectrics enhances mobility by mitigating charge trapping via dipole interactions.[28] However, existing research primarily focuses on PFG effects on carrier mobility and photogeneration, leaving a significant gap in understanding their broader impact on device functionality. Crucially, a comprehensive understanding of how PFGs simultaneously influence the integrated sensing, synaptic, and memory performance of devices remains lacking.

In this work, we present an artificial vision system based on organic-inorganic heterogeneous dielectric layers. Hafnium oxide (HfO_2) is selected as the inorganic dielectric layer due to its high dielectric constant (k), deep trap energy levels (~1.25 eV below the conduction band), and high density of charge trapping sites.[29-32] Two polymers, polyphenylene ether (PPO) and poly(4-vinylphenol) (PVP) as the buffer layers, were combined with HfO_2 to fabricate the dielectric layer, while 2-hexylthieno [4,5-b] [1] benzothieno[3,2-b][1] benzothiophene (BTBTT6-syn) served as the semiconductor layer. This configuration was designed to systematically investigate the polarity modulation effect on device performance, particularly its impact on photoresponsive, synaptic, and memory properties. Our findings reveal that polarity modulation significantly
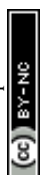
enhances the optical performance of the device, achieving improvements in key metrics such as photosensitivity (P), photoresponsivity (R), and detectivity (D^*) compared to devices employing low-polarity polymer dielectrics. Meanwhile, the use of PVP as the dielectric layer results in shorter retention times and smaller storage windows, thereby compromising the memory characteristics of the device. Despite these limitations, all kinds of devices demonstrate exceptional overall performance, including a high ON/OFF ratio ($>10^5$), good cycling endurance (700 cycles), long retention time ($>30,000$ s), and 256 multilevel memory states (8 bits). In order to explore the application of novel computing architectures in biometric recognition, we obtain palmprint images from the CASIA palmprint database and recognize them based on HfO_2-based phototransistors combined with classical machine learning algorithms. These results not only highlight the efficacy of polarity modulation in enhancing device performance but also provide a promising strategy for the development of next-generation artificial vision systems with integrated multilevel memory and built-in computation capabilities.

Results and discussion

Fig. 1a presents a simplified bioinspired artificial vision system integrating sensing, memory, and processing capabilities. To emulate the biological process where retinal neuroepithelial cells convert light into electrical impulses transmitted via neurons and synapses to the brain for processing and storage, we constructed an organic neuromorphic vision device using organic field-effect transistors (OFETs) as the fundamental building blocks. This device employs BTBTT6-syn as the UV-absorbing active layer (Fig. S1). We engineered organic-inorganic heterogeneous dielectrics using PPO or PVP blended with HfO_2 to investigate polarity effects on low-voltage operation, with single-component PVP-based and PPO-based devices serving as controls. These heterogeneous dielectrics, including PVP/HfO_2 and PPO/HfO_2, exhibit smooth surfaces with a root mean square (RMS) roughness of 0.23 nm and 0.31 nm (Fig. S2), respectively, supporting layer-by-layer BTBTT6-syn growth with comparable crystallinity and molecular ordering (Fig. S3 and S4). Therefore, the hybrid devices achieved average mobilities of 0.33 $\pm$ 0.04 cm^2 V^{-1} s^{-1} (PVP/HfO_2) and 0.31 $\pm$ 0.06 cm^2 V^{-1} s^{-1} (PPO/HfO_2), low operating voltages (-5 V), ON/OFF ratios of 10^5-10^6 (Fig. S5), and effective gate modulation (Fig. S6 and S7). Furthermore, under 365 nm illumination, photocurrent increased progressively with light intensity before saturating (Fig. 1b, c, S8a and e). Notably, PVP-based devices exhibited significantly enhanced optical metrics (Fig. S8b-d, f-h, and i-n), with their P, R and D^* values higher than PPO-based counterparts (Fig. 1d). Moreover, the temperature-dependent photoluminescence (PL) spectra of BTBTT6-syn films with PVP and PPO interfaces were measured (Fig. 1e and f). Temperature-dependent PL spectra revealed lower exciton binding energy (E_B) at the PVP interface (19.4 meV vs. 23.5 meV for PPO; Fig. 1g), calculated via Arrhenius fitting:[33]
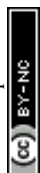
$$I(T) = I_0/(1 + Ae^{-E_B/kT})$$

where I_0 is the intensity at 0 K, T is the temperature, k is the Boltzmann constant. This confirms the reduced energy barriers for exciton dissociation into free carriers at the BTBTT6-syn/PVP interface.
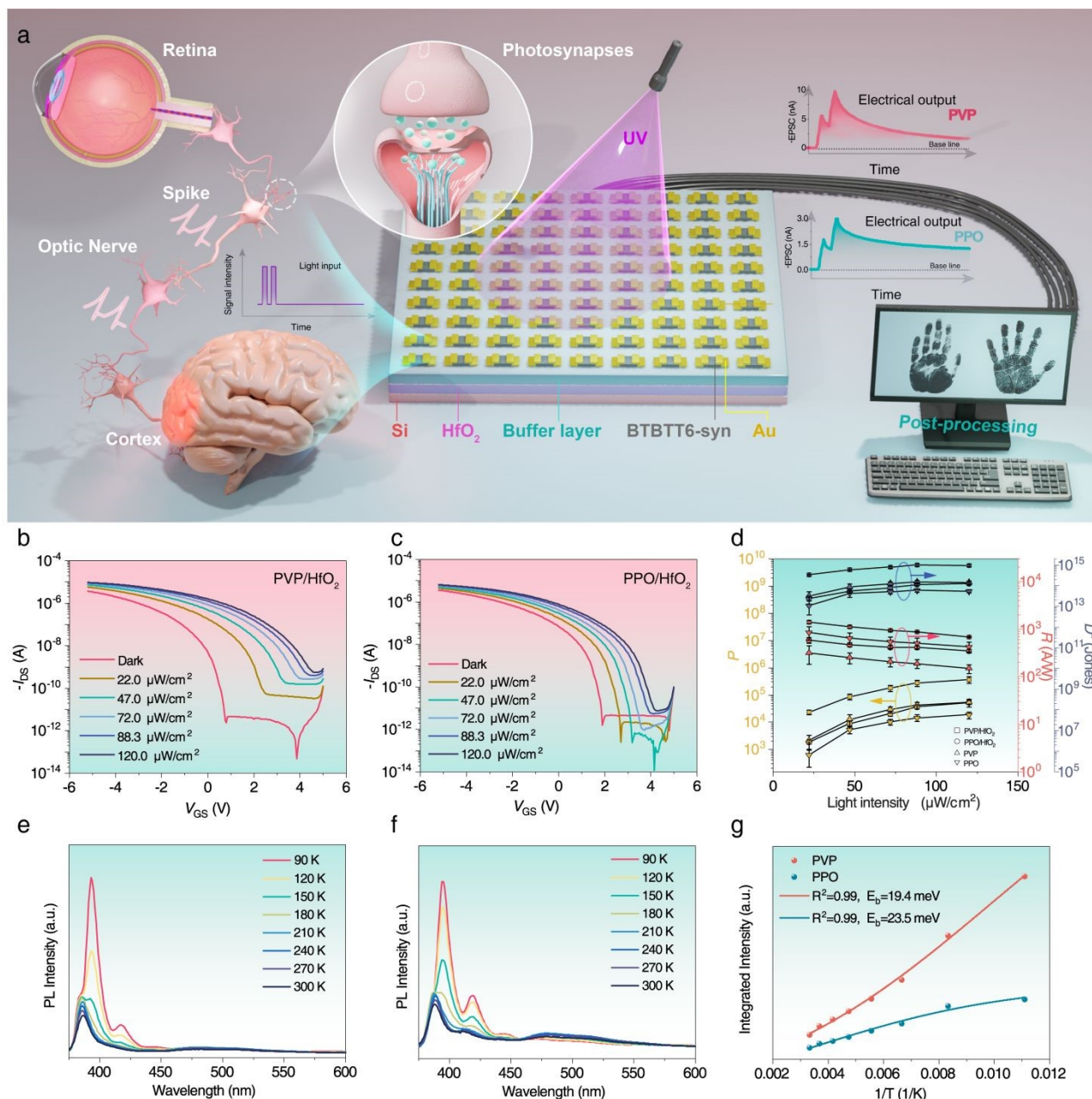
Fig. 1. (a) Organic artificial vision system with built-in memory and processing capabilities. Transfer characteristics of (b) PVP/HfO$_2$-based and (c) PPO/HfO$_2$-based organic phototransistors (OPTs) under different illumination intensities in the air. (d) P, R and D^* as a function of illumination intensity for OPTs with different dielectric layers. Temperature-dependent PL spectra for BTBTT6-syn films on (e) PVP and (f) PPO dielectrics. (g) Temperature-dependent evolution of PL integrated intensity for BTBTT6-syn films on PVP and PPO dielectrics.

Furthermore, the memory performance of the HfO$_2$-based devices was assessed. Transfer curves corresponding to electrical programming and light erasure for PVP/HfO$_2$-based and PPO/HfO$_2$-based devices are shown in Fig. 2a and b. From the curves, PPO/HfO$_2$-based device has a larger storage window (4.78 V)

than their PVP/HfO$_2$-based counterpart (2.41 V). Additionally, the dynamic memory behaviour of the devices can be modulated by multiple light pulse stimulations with a light pulse intensity of 88.3 μW/cm^2, a light pulse duration (t_{spike}) of 1 s, and a light pulse interval ($t_{interval}$) of 1 s. It is worth noting that by applying 256 light pulses, the drain currents (I_{DS}) increased significantly and showed markedly different levels up to 256 effective storage states (8-bits) of PPO/HfO$_2$-based device (Fig. 2c). The corresponding magnified curves are shown in the inset. For comparison, the 256 effective storage states (8-bit) of PVP/HfO$_2$-based device are shown in Fig. S9a. This observed multilevel memory characteristic is mainly due to variations in light pulse dosage, which modulates the concentration of photogenerated carriers in BTBTT6-syn, thereby tuning the storage states and leading to multilevel accumulation of I_{DS}. And then, the excellent durability of PVP/HfO$_2$-based and PPO/HfO$_2$-based devices is verified through consecutive electrical programming and optical erasure processes, and they can maintain a similar on/off current ratio after 700 program/erase (P/E) cycles (Fig. 2d, e, S11a, and b). Also, the retention characteristics of electrical-programmed state and light-erased state were studied (Fig. 2f and S11c), and both devices maintain good retention characteristics and are capable of sustaining 30000 seconds. The detailed working process of the device is further explained by the schematic diagram shown in Fig. 2g and S10. The device exhibits two memory states controlled by electrical programming and light erasure, respectively. Specifically, electrical-programmed state is achieved by applying a negative gate voltage (V_{GS}), during which holes in the BTBTT6-syn may be injected and trapped at the polymer/HfO$_2$ interfaces. This reduces the hole concentration in the conductive channel, causing the transfer curve to shift negatively. Light-erased state is achieved by applying a positive V_{GS} and illuminating the device with 365 nm light; Under 365 nm ultraviolet light irradiation, photogenerated excitons are formed in BTBTT6-syn, and then undergo the diffusion and dissociation. The photogenerated electrons recombine with the trapped holes, resetting the transfer curve to its initial state. [34]
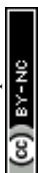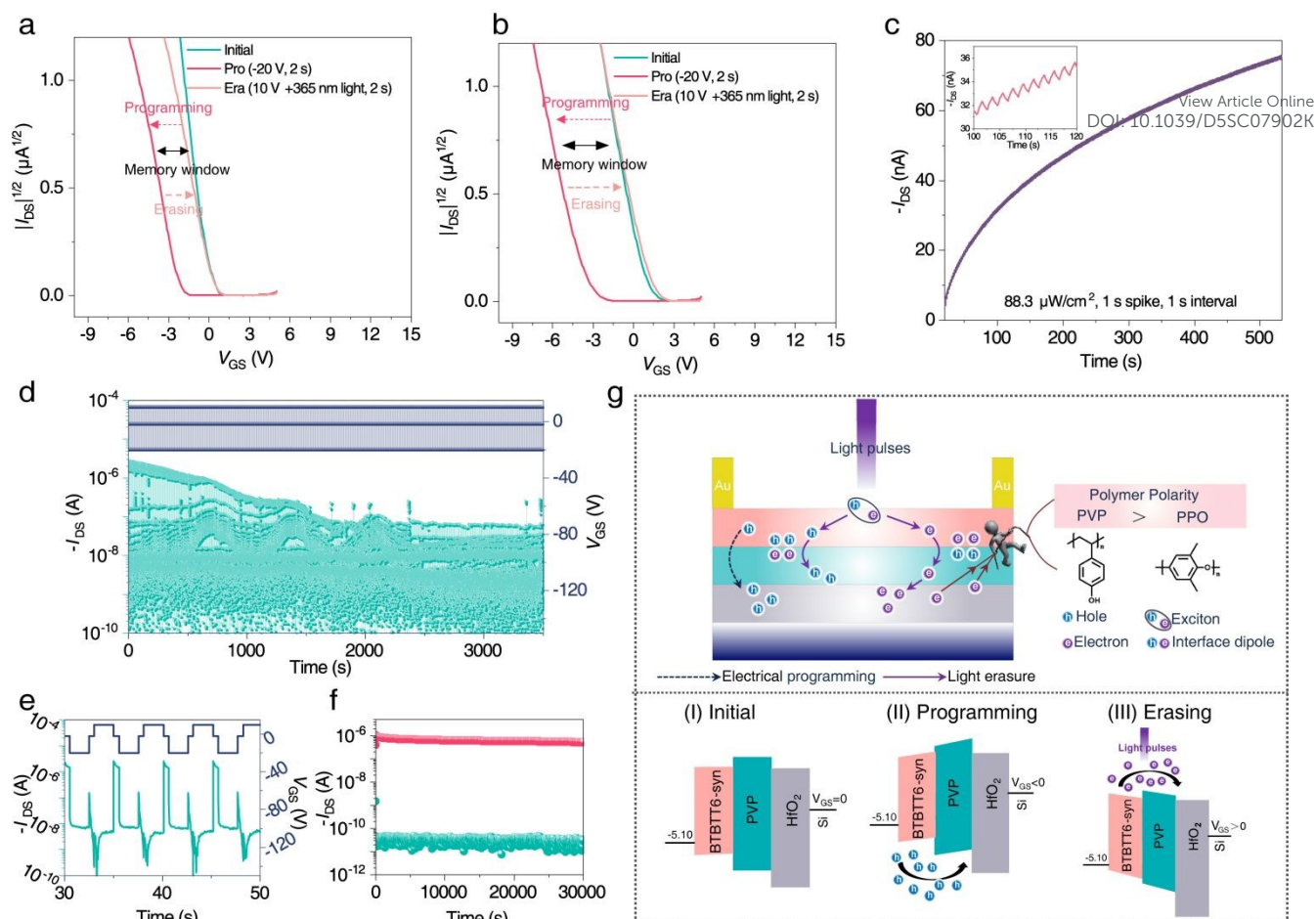
Fig. 2. Transfer curves corresponding to the initial state, electrical-programmed state, and light-erased state of (a) PVP/HfO$_2$-based and (b) PPO/HfO$_2$-based device. Electrical-programmed state was conducted at V_{GS} = -20 V with t_{spike} = 2 s, and light-erased state was achieved under a 365 nm light pulse (t_{spike} = 2 s) at V_{GS} = 10 V. (c) Multilevel memory of PPO/HfO$_2$-based device by multiple light pulse stimulations; the inset is corresponding magnified curves. (d) Endurance characteristics of the PVP/HfO$_2$-based device over 700 P/E cycles. (e) Detailed curves of the endurance characteristics of the PVP/HfO$_2$-based device, programmed at V_{GS} = -20 V with t_{spike} = 2 s, erased by a 365 nm light pulse (t_{spike} = 2 s) at V_{GS} = 10 V. (f) Retention characteristics of electrical-programmed state and light-erased state of PVP/HfO$_2$-based device. (g) Working mechanism of electrical-programmed state and light-erased state in the PVP/HfO$_2$-based device.
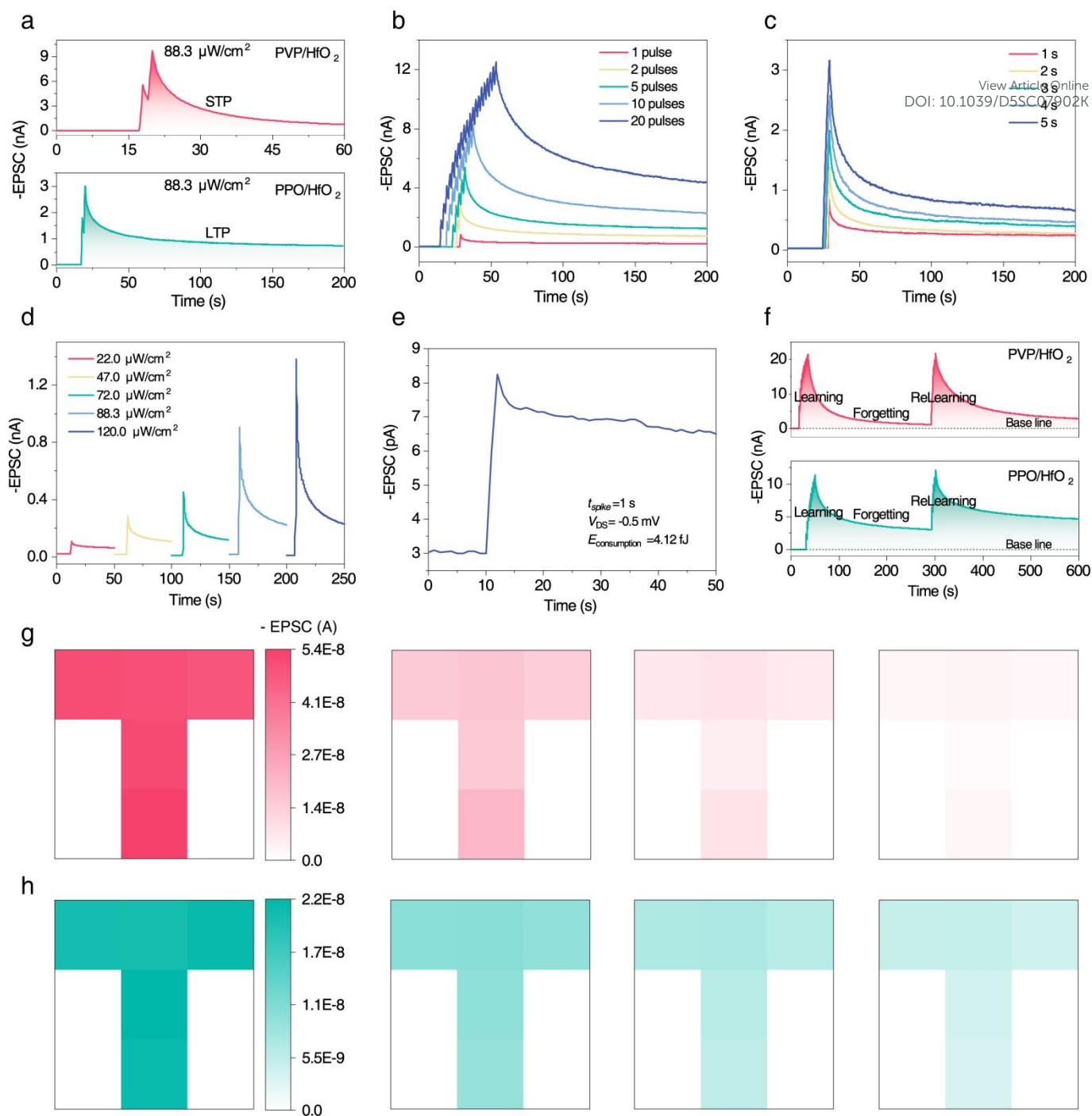
Fig. 3. (a) EPSC stimulated by two consecutive light pulses (365 nm, 88.3 μW/cm²) for PVP/HfO₂-based and PPO/HfO₂-based devices. The relationship between EPSC of PPO/HfO₂-based device and (b) light pulse number c) light pulse width (d) light pulse intensity. (e) The energy consumption of PPO/HfO₂-based device triggered by light pulses (V_{DS} = -0.5 mV, t_{spike} = 1 s). (f) The learning-forgetting-relearning process for PVP/HfO₂-based and PPO/HfO₂-based devices. Image detection and memory of light-stimulated (g) PVP/HfO₂-based and (h) PPO/HfO₂-based devices with an input image of letter T.

Subsequently, we investigated the synaptic properties of the HfO₂-based devices. Fig. 3a displays the excitatory postsynaptic current (EPSC) measured in PVP/HfO₂-based and PPO/HfO₂-based organic synaptic transistors under stimulation by two consecutive light pulses (365 nm, 88.3 μW/cm², t_{spike} = 1 s, $t_{interval}$ = 1 s) at a source-drain voltage (V_{DS}) of -1 V. Upon application of the pulses, the EPSC of the PVP/HfO₂-based
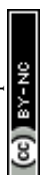
device peaked at 9.7 nA. However, 40 s after stimulation ceased, the EPSC dropped significantly to 8% (0.77 nA) of its peak value, indicating short-term potentiation (STP). In contrast, under identical stimulation, the EPSC of the PPO/HfO$_2$-based device reached a peak of 3 nA and remained above 25% (0.74 nA) of its peak value even 180 s after light removal, signifying long-term potentiation (LTP). We further modulated the EPSC of the PPO/HfO$_2$-based device by varying the number (Fig. 3b), width (Fig. 3c), and intensity (Fig. 3d) of the light pulses. While the PVP/HfO$_2$-based device also exhibited increased EPSC with higher light intensity (Fig. S12), its retention time did not extend significantly beyond that observed with a single pulse, confirming its inferior retention performance compared to the PPO/HfO$_2$-based device. Given that biological synapses operate with remarkably low energy consumption, achieving comparable energy efficiency in artificial synapses is crucial for effectively simulating human brain learning behaviors. Therefore, we measured the energy consumption per pulse under V_{DS} = -0.5 mV and t_{spike} = 1 s. The PPO/HfO$_2$-based and PVP/HfO$_2$-based devices consumed 4.12 fJ and 5.5 fJ per pulse, respectively (Fig. 3e, S13). Human memory formation follows principles like the Ebbinghaus forgetting curve,[35, 36] distinguishing between short-term memory (STM) and long-term memory (LTM) based on retention duration. Crucially, relearning after forgetting can facilitate the conversion of STM to LTM. Our devices successfully simulated this STM-to-LTM transition through a learning-forgetting-relearning process. The PPO/HfO$_2$-based device demonstrated superior relearning capability. After initial training with 10 consecutive light pulses, it required only 5 light pulses to fully recover its peak response during relearning process. In contrast, the PVP/HfO$_2$-based device required 6 light pulses to achieve full recovery (Fig. 3f). Furthermore, we achieved the image detection and memory of two different devices by using letter "T" light-stimulation. After stimulated by a light pulse of 120.0 μW/cm^2 for 10 s, EPSC reaches its peak, followed by a relatively slow forgetting process for the PPO/HfO$_2$-based devices, which ultimately maintains about 21% of the initial current after 100 s (Fig. 3g). For the PVP/HfO$_2$-based devices, the current is forgotten to about 5% of the initial current after 100 s (Fig. 3h).

To evaluate the feature mapping capability of the HfO$_2$-based devices, we performed a 4-bit light pulse stimulation (from "0000" to "1111") on the devices and measured its corresponding photocurrent. As shown in Fig. 4a, "1" and "0" represent the light state (t_{spike} = 0.5 s, $t_{interval}$ = 0.5 s, 4.71 mW/cm^2) and dark state, respectively. Fig. 4b illustrates the sampling characteristics via the I-t curves of three representative inputs, namely the I-t curves of "0011", "0111" and "1111". The I_{DS} at the output of the PVP/HfO$_2$-based and PPO/HfO$_2$-based devices under 4-bit light pulses (16 combinations) are highly dependent on the order of the light stimulus (Fig. 4c). In order to explore the application of novel computational architectures in biometric recognition, this study employs HfO$_2$-based devices combined with classical machine learning algorithms to perform recognition studies on palmprint images from the CASIA-Palmprint database. In the image preprocessing stage, an area of 240×240 pixels is intercepted from the original palmprint image based on the

center of the image to reduce the background interference and focus on the palmprint features. In the

classification model construction, five types of palmprint identities are recognized, and in order to enhance
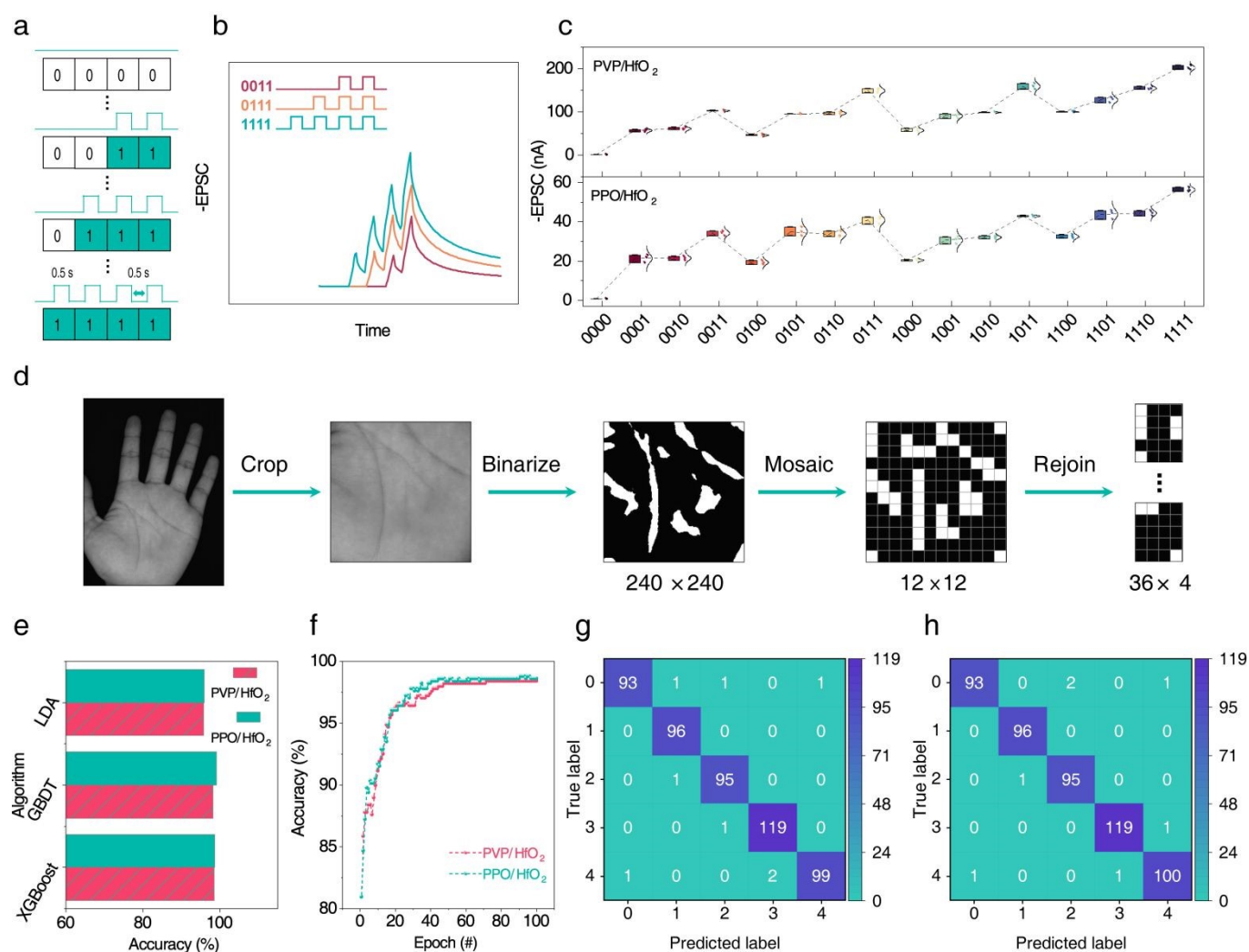
Fig. 4. (a) Device response to a 4-bit light stimulus, where "1" and "0" represent 365 nm light and dark conditions, respectively, with a light pulse width of 0.5 s and pulse interval of 0.5 s. (b) I-t light response curves for three representative inputs "0011", "0111" and "1111". (c) PVP/HfO$_2$-based and PPO/HfO$_2$-based devices in response to 4-bit light stimulus. (d) Pre-processing of the palmprint images, including cropping, binarizing, mosaic and rejoining. (e) The accuracy of three different algorithms based on PVP/HfO$_2$-based and PPO/HfO$_2$-based devices. (f) Evolution of accuracy based on PVP/HfO$_2$-based and PPO/HfO$_2$-based devices. (g) The confusion matrix of PVP/HfO$_2$-based device shows accurate classification and misclassification. (h) The confusion matrix of PPO/HfO$_2$-based device shows accurate classification and misclassification.

the robustness of the model, the sample data are extended by introducing various forms of noise, and a total

of 850 image samples are generated (Fig. S14). Subsequently, the samples are processed with bilateral filtering

for noise reduction, CLAHE for contrast enhancement, adaptive threshold binarization, and closed-

computation to obtain binarized images that are convenient for HfO$_2$-based devices transformation. In the

feature extraction stage, the spatial block statistics method is used to divide the preprocessed binarized image into 20×20 grids, and the percentage of white pixels within each grid is calculated to form a 12×12 feature matrix. This matrix is binary converted and input into the HfO_2-based devices in units of four pixels, and each group sequences is mapped into photocurrent eigenvalues, and a standardized 36-dimensional eigenvector is finally generated (Fig. 4d). Three classical algorithms, linear discriminant analysis (LDA), gradient boosting decision tree (GBDT) and eXtreme Gradient Boosting (XGBoost), are selected for the experiment, and the evaluation metrics is recognition accuracy. As shown in Fig. 4e, the integrated tree models with PVP/HfO_2-based and PPO/HfO_2-based devices exhibit superior recognition performance. Specifically, Gradient Boosting Decision Tree (GBDT) achieves the highest accuracy of 99.02% on PPO/HfO_2-based devices, eXtreme Gradient Boosting (XGBoost) maintains more than 98.43% performance on both devices, while linear discriminant analysis (LDA) is only 95.69% and 95.88% on PVP/HfO_2-based and PPO/HfO_2-based devices. The results show that the optoelectronic features extracted by the HfO_2-based devices are significantly differentiable, in which the nonlinear modelling capabilities of GBDT and XGBoost can effectively capture the palm texture features. Furthermore, based on the XGBoost, PVP/HfO_2-based and PPO/HfO_2-based devices achieve 98.43% and 98.63% accuracy, respectively, after 100 training sessions, and both have similar convergence speeds (Fig. 4f). Lastly, the accuracy of PVP/HfO_2-based and PPO/HfO_2-based devices was evaluated in detail, and the results are presented in the form of a confusion matrix (Fig. 4g, h).

Conclusion

In summary, we have developed a novel neuromorphic vision system based on polarity-engineered HfO_2 phototransistors, which integrates optical sensing, synaptic plasticity, and nonvolatile memory functions in a single device. Through systematic investigation of polar polymer dielectric layers, we demonstrate that interfacial polarity modulation simultaneously enhances photoresponsivity while presenting a fundamental trade-off with charge retention characteristics. The optimized devices achieve high performance metrics, including an ultrahigh ON/OFF ratio ($>10^5$), excellent endurance (700 cycles), prolonged retention ($>30,000$ s), and 256 distinct conductance states (8-bit precision). And the feasibility of novel sensing architecture combined with traditional machine learning algorithms in biometrics recognition is verified, which provides a new idea to break through the bottleneck of storage-computing separation, and the heterogeneous computational architectures of convolutional neural networks and devices can be explored in the future to enhance the ability of complex pattern recognition. This work not only provides fundamental insights into polarity-dependent charge transport mechanisms but also establishes a materials design paradigm for next-generation neuromorphic devices.
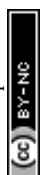
Methods

Materials

PVP and PPO were purchased from Sigma-Aldrich. The BTBTT6-syn was synthesized based on previous literature[37].

Device fabrication

HfO_2 thin films were deposited on Si substrates via plasma-enhanced atomic layer deposition (PEALD) at Beijing Jiaotong University, using a Beneq TFS-200 system. The deposition process employed tetrakis (dimethylamino) hafnium (TDMAH) as the metal precursor and deionized water as the oxygen source, with the chamber temperature maintained at 200°C during the growth process. The deposited HfO_2 crystals are thermodynamically stable monoclinic phases that are intrinsically non-ferroelectric. The thickness of the prepared HfO_2 thin film is 15 nm. Subsequently, HfO_2 was treated with O_2 plasma (50 W, 5 min) and spin-coated with a 6 mg/ml solution of PVP and PPO (Fig. S15), respectively, for the preparation of organic-inorganic dielectrics. On the other hand, ITO was treated with O_2 plasma (50 W, 5 min) and spin-coated with a 30 mg/ml solution of PVP and PPO, respectively, for preparing single-component dielectrics. Among them, the PPO dielectrics were annealed at 80 °C for 30 min. The above spin-coating and annealing were done in N_2 environment provided by the glove box. ITO glass substrates used in this experiment were cleaned with deionized water, acetone and isopropanol, and then dried with nitrogen. The plasma treatment was carried out using NAEN TECH. Then, 20 nm BTBTT6-syn film was deposited on different dielectric layers at a rate of 0.05 Å s^{-1} in a vacuum of 1×10^{-5} Pa without external substrate heating. Finally, 20 nm Au film was deposited on the surface of the semiconductor layers at a rate of 0.06 Å s^{-1} as source/drain electrodes. The prepared devices were all bottom-gate top-contact OFETs. The capacitance of PVP/HfO_2-based and PPO/HfO_2-based dielectrics was measured as 102.3 nF/cm^2 and 74.7 nF/cm^2, respectively (Fig. S16).

Measurements

Using a Micromanipulator 6150 probe station and a Keithley 2636B semiconductor parameter analyzer, the electrical properties were examined in the air. Utilizing a semiconductor analyzer and a commercial LED with an optical filter of 365 nm, optoelectronic properties were measured. Gala Instrument Prep$_2$ was used to perform the plasma treatment. Atomic force microscopy (AFM) tests were performed using a Bruker Dimension Icon microscope in tapping mode. UV absorption spectroscopy measurements were carried out using a SHIMADZU UV-3600 Plus spectrometer. Rigaku Smartlab diffractometer operating in reflection mode at 45 kV and 200 mA was used to perform XRD measurements. The capacitance was measured by the
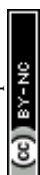
PDA FS360.

Conflict of interest

The authors declare no competing interests.

Data availability statements

Data are available upon request from the authors.

Acknowledgements

References

1. E. J. Fuller, S. T. Keene, A. Melianas, Z. Wang, S. Agarwal, Y. Li, Y. Tuchman, C. D. James, M. J. Marinella, J. J. Yang, A. Salleo and A. A. Talin, Parallel programming of an ionic floating-gate memory array for scalable neuromorphic computing, *Science*, 2019, **364**, 570-574.
2. D. Ielmini and H. S. P. Wong, In-memory computing with resistive switching devices, *Nat. Electron.*, 2018, **1**, 333-343.
3. K. Roy, A. Jaiswal and P. Panda, Towards spike-based machine intelligence with neuromorphic computing, *Nature*, 2019, **575**, 607-617.
4. Y. van de Burgt, E. Lubberman, E. J. Fuller, S. T. Keene, G. C. Faria, S. Agarwal, M. J. Marinella, A. Alec Talin and A. Salleo, A non-volatile organic electrochemical device as a low-voltage artificial synapse for neuromorphic computing, *Nat. Mater.*, 2017, **16**, 414-418.
5. Q. Xia and J. J. Yang, Memristive crossbar arrays for brain-inspired computing, *Nat. Mater.*, 2019, **18**, 309-323.
6. L. Danial, E. Pikhay, E. Herbelin, N. Wainstein, V. Gupta, N. Wald, Y. Roizin, R. Daniel and S. Kvatinsky, Two-terminal floating-gate transistors with a low-power memristive operation mode for analogue neuromorphic computing, *Nat. Electron.*, 2019, **2**, 596-605.
7. S. Chen, Z. Lou, D. Chen and G. Shen, An Artificial Flexible Visual Memory System Based on an UV-Motivated Memristor, *Adv. Mater.*, 2018, **30**, 1705400.
8. X. Hou, C. Liu, Y. Ding, L. Liu, S. Wang and P. Zhou, A Logic-Memory Transistor with the Integration of Visible Information Sensing-Memory-Processing, *Adv. Sci.*, 2020, **7**, 2002072.
9. A. Melianas, T. J. Quill, G. LeCroy, Y. Tuchman, H. v. Loo, S. T. Keene, A. Giovannitti, H. R. Lee, I. P. Maria, I. McCulloch and A. Salleo, Temperature-resilient solid-state organic artificial synapses for neuromorphic computing, *Sci. Adv.*, 2020, **6**, eabb2958.
10. M. D. Tran, H. Kim, J. S. Kim, M. H. Doan, T. K. Chau, Q. A. Vu, J.-H. Kim and Y. H. Lee, Two-Terminal Multibit Optical Memory via van der Waals Heterostructure, *Adv. Mater.*, 2019, **31**, 1807075.
11. D. Xiang, T. Liu, J. Xu, J. Y. Tan, h. Zehua, B. Lei, Y. Zheng, A. Castro Neto, L. Liu and W. Chen, Two-dimensional multibit optoelectronic memory with broadband spectrum distinction, *Nat. Commun.*, 2018, **9,** 2966.
12. Q. Wang, Y. Wen, K. Cai, R. Cheng, L. Yin, Y. Zhang, J. Li, Z. Wang, F. Wang, F. Wang, T. A. Shifa, C. Jiang, H. Yang and J. He, Nonvolatile infrared memory in MoS2/PbS van der Waals heterostructures, *Sci. Adv.*, 2018, **4**, eaap7916.

13.   L. Wang, C. Zheng, J. Fu, J. Hua, J. Chen, J. Gao, H. Ling, L. Xie and W. Huang, Influence of Molecular Weight of Polymer Electret on the Synaptic Organic Field-Effect Transistor Performance, *Adv. Electron. Mater.*, 2022, **8**, 2200155.

14.   D. Li, N. An, K. Tan, Y. Ren, H. Wang, S. Li, Q. Deng, J. Song, L. Bu and G. Lu, Insulating Electrets Converted from Organic Semiconductor for High-Performance Transistors, Memories, and Artificial Synapses, *Adv. Funct. Mater.*, 2023, **33**, 2305012.

15.   K. Chen, H. Hu, I. Song, H. B. Gobeze, W.-J. Lee, A. Abtahi, K. S. Schanze and J. Mei, Organic optoelectronic synapse based on photon-modulated electrochemical doping, *Nat. Photonics*, 2023, **17**, 629-637.

16.   C. Wang, H. Dong, L. Jiang and W. Hu, Organic semiconductor crystals, *Chem. Soc. Rev.*, 2018, **47**, 422-500.

17.   B. Wang, W. Huang, L. Chi, M. Al-hashimi, T. Marks and A. Facchetti, High-k Gate Dielectrics for Emerging Flexible and Stretchable Electronics, *Chem. Rev.*, 2018, **118,** 5690-5754.

18.   H. Chen, W. Zhang, M. Li, G. He and X. Guo, Interface Engineering in Organic Field-Effect Transistors: Principles, Applications, and Perspectives, *Chem. Rev.*, 2020, **120**, 2879-2949.

19.   C.-H. Wang, C.-Y. Hsieh and J.-C. Hwang, Flexible Organic Thin-Film Transistors with Silk Fibroin as the Gate Dielectric, *Adv. Mater.*, 2011, **23**, 1630-1634.

20.   K. Shi, W. Zhang, D. Gao, S. Zhang, Z. Lin, Y. Zou, L. Wang and G. Yu, Well-Balanced Ambipolar Conjugated Polymers Featuring Mild Glass Transition Temperatures Toward High-Performance Flexible Field-Effect Transistors, *Adv. Mater.*, 2018, **30**, 1705286.

21.   J. Xu, S. Wang, G.-J. N. Wang, C. Zhu, S. Luo, L. Jin, X. Gu, S. Chen, V. R. Feig, J. W. F. To, S. Rondeau-Gagné, J. Park, B. C. Schroeder, C. Lu, J. Y. Oh, Y. Wang, Y.-H. Kim, H. Yan, R. Sinclair, D. Zhou, G. Xue, B. Murmann, C. Linder, W. Cai, J. B.-H. Tok, J. W. Chung and Z. Bao, Highly stretchable polymer semiconductor films through the nanoconfinement effect, *Science*, 2017, **355**, 59-64.

22.   F. A. Viola, J. Barsotti, F. Melloni, G. Lanzani, Y.-H. Kim, V. Mattoli and M. Caironi, A sub-150-nanometre-thick and ultraconformable solution-processed all-organic transistor, *Nat. Commun.*, 2021, **12**, 5842.

23.   Y. Wang, X. Huang, T. Li, L. Li, X. Guo and P. Jiang, Polymer-Based Gate Dielectrics for Organic Field-Effect Transistors, *Chem. Mater.*, 2019, **31**, 2212-2240.

24.   S. Lee, B. Koo, J. Shin, E. Lee, H. Park and H. Kim, Effects of hydroxyl groups in polymeric dielectrics on organic transistor performance, *Appl. Phys. Lett.*, 2006, **88**, 162109.

25.   G.-M. Ko, Y. G. Kang, U.-C. Jeong, T.-W. Lee and H.-L. Park, Polymeric gate insulators to induce synaptic photoresponse of organic transistors, *J. Korean Phys. Soc.*, 2023, **83**, 320-327.

26.   Y. Liu, Q. Chen, Y. Guo, B. Guo, G. Liu, Y. Liu, L. He, Y. Li, J. He and M. Tang, Enhancing the Uniformity of a Memristor Using a Bilayer Dielectric Structure, *Micromachines*, 2024, **15**, 605.

27.   D. Ji, T. Li, Y. Zou, M. Chu, K. Zhou, J. Liu, G. Tian, Z. Zhang, X. Zhang, L. Li, D. Wu, H. Dong, Q. Miao, H. Fuchs and W. Hu, Copolymer dielectrics with balanced chain-packing density and surface polarity for high-performance flexible organic electronics, *Nat. Commun.*, 2018, **9**, 2339.

28.   H. Li, T. Jiang, Y. Zheng, Y. Zou, S. Qi, G. Tian, D. Ji, L. Li and W. Hu, Fluorinated Dielectrics-Modulated Organic Phototransistors and Flexible Image Sensors, *Adv. Opt. Mater.*, 2022, **10**, 2200614.

29.   T. Hasan, S. Zafar, E. Ozbay and A. U. Kashif, Analysis of HfO2 and ZrO2 as High-K Dielectric for CMOS Nano Devices. in 2022 9th International Conference on Electrical and Electronics Engineering (ICEEE) (IEEE, Alanya, Turkey, 2022), 99–103.

30.   J. H. Choi, Y. Mao and J. P. Chang, Development of hafnium based high-k materials—A review, *MAT SCI ENG R*, 2011, **72**, 97-136.

31.   G. Molas, M. Bocquet, E. Vianello, L. Perniola, H. Grampeix, J. P. Colonna, L. Masarotto, F. Martin, P. Brianceau, M. Gély, C. Bongiorno, S. Lombardo, G. Pananakakis, G. Ghibaudo and B. De Salvo, Reliability of charge trapping memories with high-k control dielectrics (Invited Paper), *Microelectron. Eng.*, 2009, **86**, 1796-1803.

32.   V. A. Gritsenko, T. V. Perevalov and D. R. Islamov, Electronic properties of hafnium oxide: A contribution from defects and traps, *Phys. Rep.*, 2016, **613**, 1-20.

33.   L. Zhu, J. Zhang, Y. Guo, C. Yang, Y. Yi and Z. Wei, Small Exciton Binding Energies Enabling Direct Charge
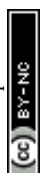
Photogeneration Towards Low-Driving-Force Organic Solar Cells, *Angew. Chem. Int. Ed.*, 2021, **60**, 15348-15353.

34.   K.-J. Baeg, Y.-Y. Noh, J. Ghim, B. Lim and D.-Y. Kim, Polarity Effects of Polymer Gate Electrets on Non-Volatile Organic Field-Effect Transistor Memory, *Adv. Funct. Mater.*, 2008, **18**, 3678-3685.

35.   D. G. Roe, S. Kim, Y. Y. Choi, H. Woo, M. S. Kang, Y. J. Song, J. H. Ahn, Y. Lee and J. H. Cho, Biologically Plausible Artificial Synaptic Array: Replicating Ebbinghaus' Memory Curve with Selective Attention, *Adv Mater*, 2021, **33**, e2007782.

36.   S. G. Hu, Y. Liu, T. Chen, Z. Liu and Q. Yu, Emulating the Ebbinghaus forgetting curve of the human brain with a NiO- based memristor, *Appl. Phys. Lett.*, 2013, **103**, 133701.

37.   T. Jiang, Y. Wang, Y. Zheng, L. Wang, X. He, L. Li, Y. Deng, H. Dong, H. Tian, Y. Geng, L. Xie, Y. Lei, H. Ling, D. Ji and W.Hu, *Nat. Commun.* 2023, **14**, 2281.

Chemical Science Accepted Manuscript

Data availability statements

Data are available upon request from the authors.

Chemical Science Accepted Manuscript